Crystal structure and magnetism in α-$RuCl_3$: An *ab initio* study

Heung-Sik Kim[1] and Hae-Young Kee[1,2,*]

[1]*Department of Physics and Center for Quantum Materials, University of Toronto, 60 St. George Street, Toronto, Ontario, Canada M5S 1A7*

[2]*Canadian Institute for Advanced Research/Quantum Materials Program, Toronto, Ontario, Canada MSG 1Z8*

(Received 22 September 2015; revised manuscript received 8 March 2016; published 22 April 2016)

α-$RuCl_3$ has been proposed recently as an excellent playground for exploring Kitaev physics on a two-dimensional (2D) honeycomb lattice. However, structural clarification of the compound has not been completed, which is crucial in understanding the physics of this system. Here, using *ab initio* electronic structure calculations, we study a full three-dimensional (3D) structure of α-$RuCl_3$, including the effects of spin-orbit coupling (SOC) and electronic correlations. The three major results are as follows: (i) SOC suppresses dimerization of Ru atoms, which exists in other Ru compounds such as isostructural Li_2RuO_3, and makes the honeycomb closer to an ideal one. (ii) The nearest-neighbor Kitaev exchange interaction between the $j_{\text{eff}} = 1/2$ pseudospin strongly depends on the Ru-Ru distance and the Cl position, originating from the nature of the edge-sharing geometry. (iii) The optimized 3D structure without electronic correlations has $P\bar{3}1m$ space-group symmetry independent of SOC, but including electronic correlation changes the optimized 3D structure to either $C2/m$ or $Cmc2_1$ within 0.1 meV per formula unit (f.u.) energy difference. The reported $P3_112$ structure is also close in energy. The interlayer spin-exchange coupling is a few percent of the in-plane spin-exchange terms, confirming that α-$RuCl_3$ is close to a 2D system. We further suggest how to increase the Kitaev term via tensile strain, which sheds light in realizing the Kitaev spin-liquid phase in this system.

DOI: 10.1103/PhysRevB.93.155143

I. INTRODUCTION

There have been a number of studies on quasi-two-dimensional systems having both spin-orbit coupling (SOC) and on-site Coulomb interactions, which are believed to host unconventional magnetic orders and spin-liquid phases [1,2]. One promising candidate is α-$RuCl_3$, where edge-sharing $RuCl_6$ octahedra form two-dimensional $RuCl_3$ layers in which Ru honeycomb layers reside [3–11]. Compared to its $5d$ transition-metal-oxide counterparts α-A_2IrO_3 (A = Li, Na) [12–16], α-$RuCl_3$ has closer-to-ideal $RuCl_6$ octahedra [3], so it was proposed as an excellent platform to explore the Kitaev physics and related magnetism despite weaker SOC [4,9,11,17,18]. A few recent reports suggest the presence of strong Kitaev-type bond-dependent exchange interactions in α-$RuCl_3$ [5], which originate from the cooperation between the intermediate SOC in the Ru atom and the Coulomb interaction [8]. A zigzag-type magnetic order within the $RuCl_3$ layer is also predicted and observed, which is proximate to the Kitaev spin-liquid phase [5,8].

In previous studies, α-$RuCl_3$ was considered as a two-dimensional system with an ideal Ru honeycomb lattice, but such assumption needs further clarification. A potential Ru layer distortion, which is observed in an isostructural compound Li_2RuO_3 [19,20], might happen in this compound. Furthermore, α-$RuCl_3$ has a three-dimensional crystal structure consisting of $RuCl_3$ layer stacking, and interlayer coupling and interaction terms can introduce another complication. Experimentally, both $P3_112$ and $C2/m$ space groups have been suggested as the crystalline symmetry in this compound [3,6,11,21,22]. As an illustrative example, Fig. 1(a) shows the crystal structure of α-$RuCl_3$ with a $C2/m$ space-group symmetry, where adjacent $RuCl_3$ layers within the unit cell are related to each other by a translation along the a axis in the figure. Stacking faults can easily be introduced in this layered structure as in the case of α-A_2IrO_3 [23], which obscures further clarification of the crystal structure. The effect of interlayer exchange interactions from the layer stacking on the ground-state magnetic properties of this system is not well understood either. More interestingly, a sample-dependent two-transition behavior is reported, where two different magnetic order peaks at $T_{N1} \simeq 14$ K and $T_{N2} \simeq 8$ K with two- and three-layer c-axis periodicity, respectively, are observed in neutron-diffraction measurement [11]. These issues pose a question on the relation between crystal structure and magnetism in this system.

In pursuit of such motivations, in this work we perform *ab initio* calculations for the structural properties of α-$RuCl_3$ and their impact on magnetism. We present three main results: (i) The role of SOC and zigzag magnetic order on the single-layer $RuCl_3$ structure is discussed. We find that SOC prefers an ideal honeycomb lattice by preventing Ru-Ru dimer formations, and the presence of in-plane zigzag order tends to give small monoclinic distortion commensurate with the magnetic order. (ii) The effect of Ru-Cl and Ru-Ru distance on the exchange interactions and magnetism is discussed, where the hopping channels within the nearest-neighbor (NN) Ru t_{2g} orbitals and the resulting exchange interactions between the SOC-induced $j_{\text{eff}} = 1/2$ pseudospins strongly depend on the Ru-Cl and Ru-Ru distance. Such behavior originates from the existence of multiple hopping channels in the t_{2g} orbitals, which enables *leveraging* magnetism with rather small amount of structural changes. (iii) The stability of crystal structures with different stacking orders is discussed by comparing relative total energies. We find that structures with $C2/m$ [22] and $Cmc2_1$ space-group symmetries are most favorable with almost degenerate energies. The previously suggested $P3_112$ structure [3,21] yields total energy comparable to those of $C2/m$ and $Cmc2_1$ structures, with the energy

*hykee@physics.utoronto.ca

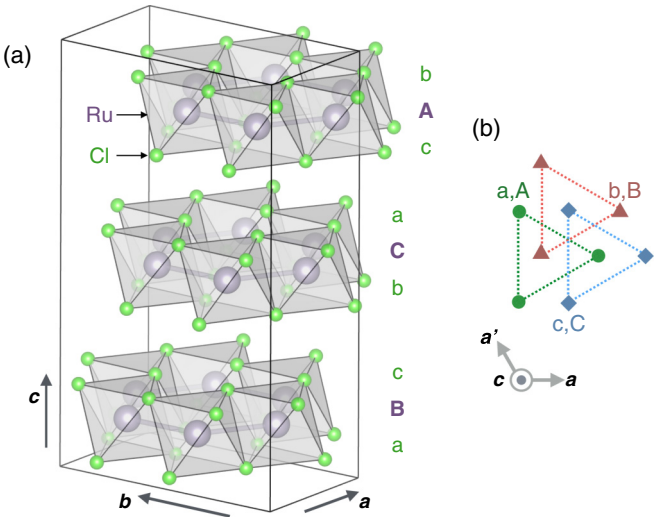

FIG. 1. (a) Crystal structure of α-$RuCl_3$ with the $C2/m$ space group. Solid lines depict a monoclinic unit cell. (b) Schematic view of three triangular sublattices on which Ru and Cl layers are located. Stacking indices for Ru honeycomb and Cl triangular layers are shown on the right side of (a), where indices for Ru and Cl layers are expressed as capital and lowercase letters, respectively.

difference smaller than 0.4 meV per formula unit (f.u.). Energy differences between different interlayer magnetic orders are smaller than 0.1 meV/f.u., and the magnitude of interlayer exchange interactions estimated from interlayer hopping integrals is smaller than 0.05 meV. These observations justify the employment of two-dimensional spin models in exploring magnetism in α-$RuCl_3$. We further propose how to increase the Kitaev term using tensile strain or uniaxial pressure to realize the Kitaev spin-liquid phase.

This paper is organized as follows. After showing computational details in Sec. II, the structural properties of single-layer $RuCl_3$ and its relation to magnetism are presented in Sec. III. The effect of SOC and zigzag magnetic order on the single-layer $RuCl_3$ structure, and the relation between the structure and magnetism, are discussed in Secs. III A and III B, respectively. In Secs. IV and V, the results on the stacking without and with the Coulomb interaction and magnetism are shown, respectively. A summary and conclusion follow in Sec. VI.

II. COMPUTATIONAL DETAILS

For the electronic structure calculations, we employed the Vienna *ab initio* Simulation Package (VASP), which uses the projector augmented wave (PAW) basis set [24,25]. 370 eV of plane-wave energy cutoff was used and, for k-point sampling, a 15×15 and $8 \times 6 \times 4(6)$ Monkhorst-Pack grid was adopted for single-layer primitive cell and monoclinic cells with three- (two)-layer c-axis periodicity. The tetrahedron method with Blöchl correction was used for the calculation of density of states [26]. On-site Coulomb interactions are incorporated using the Dudarev's rotationally invariant DFT+U formalism [27] with effective $U_{\rm eff} \equiv U - J = 2$ eV. For each configuration with different unit cell, $U_{\rm eff}$ value, and magnetic order, structural optimization is performed with a force criterion of 1 meV/Å. Unless specified, a revised Perdew-Burke-Ernzerhof generalized gradient approximation (PBEsol) [28] was used for structural optimization and total-energy calculations. Note that the PBEsol functional yielded reasonable results for the stacking order of bilayer transition-metal dichalcogenides in comparison to the van der Waals functionals [29]. The results from employing vdW functionals are shown in the Appendix. Interlayer hopping integrals were obtained by employing maximally localized Wannier orbital formalism (MLWF) [30,31] implemented in the WANNIER90 package [32]. Also, for comparison of the magnetism in the single-layer structures in Sec. III, a linear-combination-of-pseudo-atomic-orbital basis code OPENMX [33,34] was used, where double-zeta plus polarization (DZP) bases, 500 Ry of energy cutoff for real-space integrations, and the Perdew-Zunger parametrization for the local-density approximation were employed [35,36].

III. RELATION BETWEEN STRUCTURE AND MAGNETISM IN $RuCl_3$ SINGLE LAYER

In this section, structural changes due to the lattice optimization and their effect on the magnetism are discussed in the $RuCl_3$ single layer. The initial trial structure we chose is the one reported in Ref. [37], which was used in Ref. [8]. The lattice optimization gives rise to in-plane structural changes, and here we present the optimized structures focusing on the difference from the old one. Since we found that such behavior and the resulting changes in magnetism also occur in the full three-dimensional (3D) structures, which are presented in Secs. IV and V, below we first discuss the single-layer results.

A. Effect of SOC on in-plane Ru dimerization

First, the effect of SOC and magnetism with $U_{\rm eff}$ on a Ru honeycomb lattice is discussed in this section. Figure 2 summarizes the results, where the sizes of Ru displacements δ from the ideal honeycomb lattice after structural optimizations under different conditions are shown. Positive and negative values of δ in Fig. 2(b) correspond to Ru dimerization and Ru zigzag-chain formation, respectively, as shown in Fig. 2(a). Note that the lattice constants are fixed to the experimentally observed $a = a_0 = 5.96$ Å and $b = \sqrt{3}a_0$. Without including SOC and Coulomb interactions, the two Ru atoms in the unit cell tend to dimerize to lower the energy, as shown in Fig. 2(a). The presence of dimer formation is robust against different choices of exchange-correlation functionals—Perdew-Zunger parametrization of local-density approximation (LDA) [36], PBE [38], and PBEsol—with slightly different size of δ, as shown in Fig. 2(b). Similar dimer formation was reported in another layered honeycomb compound, Li_2RuO_3, whose origin is suggested to be the σ-like direct bonding between the neighboring Ru t_{2g} orbitals [19,20].

Since the dimer formation breaks the Ru t_{2g} degeneracy, we expect that SOC would not favor the dimer formation. The spin-orbit entangled $j_{\rm eff}$ orbitals, which emerge under the presence of cubic crystal fields and SOC [39,40], do not favor orbital polarization between the t_{2g}—d_{xy}, d_{xz}, and d_{yz}—orbitals. Indeed, structural optimizations including SOC yield significant reduction of dimerization, as shown in the middle of Fig. 2(b). Although there are small differences

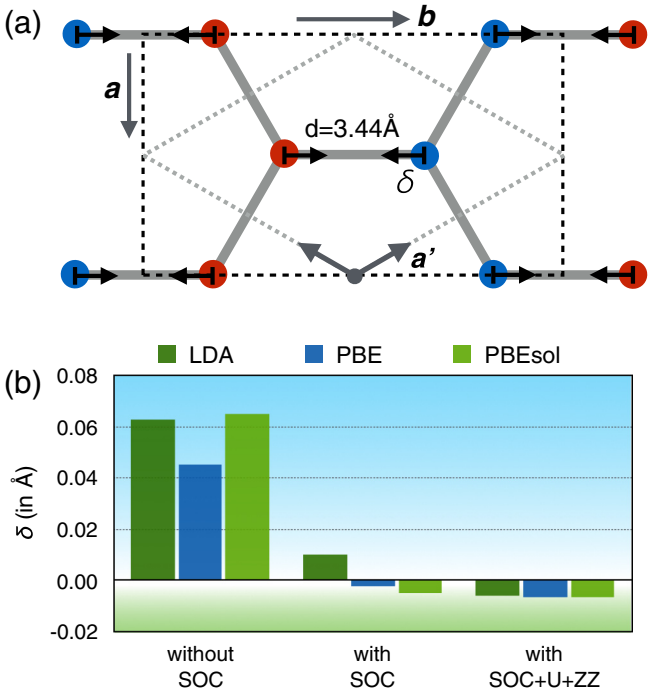

FIG. 2. (a) Schematic figure of Ru honeycomb with colored circles depicting Ru sites. Gray dotted and black dashed squares represent the primitive and monoclinic unit cells, respectively, where colors on Ru sites show the zigzag magnetic order in a monoclinic unit cell. (b) Size of Ru distortion δ under different exchange-correlation functionals and with/without the presence of SOC, U_{eff}, and in-plane zigzag magnetic order. Note that positive and negative δ correspond to Ru dimer and zigzag-chain formations, respectively.

between LDA, PBE, and PBEsol results, the role of SOC in preventing the dimerization is evident. Additionally, inclusion of the on-site Coulomb interaction without the presence of magnetism is expected to enhance the idealness of the Ru honeycomb lattice, since it was shown previously that the on-site Coulomb interaction effectively enhances the size of SOC [8,41].

Next we show the effect of in-plane zigzag magnetic order, which is predicted to occur when SOC and the Coulomb interaction are incorporated into *ab initio* calculations [8] and observed in experiments [5,11]. The right columns of Fig. 2(b) show the results from calculations including SOC, $U_{\text{eff}} = 2$ eV, and the zigzag order. The enlarged monoclinic unit cell and the magnetic configuration are shown in Fig. 2(a), where the red and blue colored circles represent Ru sites with antiparallel moments to each other. Regardless of the choice of functional, δ shows negative values with almost the same magnitude. The resulting structure is commensurate to the zigzag magnetic order, as shown in Fig. 2(a), suggesting a finite magnetoelastic coupling in this compound.

B. Effects of Cl displacement and lattice constant change to the exchange interactions between the $j_{\text{eff}} = 1/2$ pseudospins

Here we discuss the Cl displacement after the optimization and its impact on the exchange interactions between the neighboring Ru $j_{\text{eff}} = 1/2$ pseudospins. Figure 3 shows the

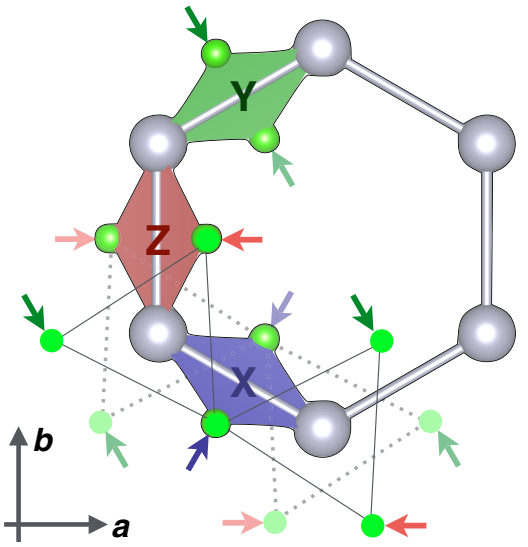

FIG. 3. Schematic figure showing the direction of Cl displacement from the ideal position after the structural optimization. Three inequivalent NN bonds—*Z*, *X*, and *Y* bonds—and the displacements of participating Cl atoms therein are depicted by red, blue, and green planes and arrows, respectively. Cl triangles located above and below the Ru plane are represented as solid and dotted triangles, respectively.

displacement of Cl atoms after structural optimization, where the two Cl atoms participating in each NN Ru bond move toward the bond center. When the in-plane lattice constants are fixed to be $a = a_0$ and $b = \sqrt{3}a_0$, structural optimization with SOC only (no U_{eff} and magnetism) yields reduced Cl height of 1.43 to 1.34 Å with respect to the Ru plane, and the Cl triangles above and below the Ru plane rotate by 2.7° in the opposite direction as shown in the figure. The Ru-Cl-Ru NN bond angle increases from 89.1° to 93.8°. After allowing the lattice constants to relax, the lattice constants reduce to $a = 0.981a_0$ and $b = 0.986b_0$ when SOC is employed with the monoclinic distortion allowed. With $U_{\text{eff}} = 2$ eV and the zigzag magnetic order, they are increased to $a = 1.011a_0$ and $b = 1.006b_0$. The averaged Ru-Cl distance changes from 2.34 to 2.36 Å in the nonmagnetic calculation, with $U_{\text{eff}} = 0$ eV, to the magnetic results, with $U_{\text{eff}} = 2$ eV, but both of them are shorter than the distance of 2.45 Å in the initial trial structure. Note that when the monoclinic distortion is allowed, the NN *Z* bond in Fig. 3 becomes inequivalent to the *X* and *Y* bonds, where the *X* and *Y* bonds form the zigzag chain in Fig. 2(a). Also, no Ru-Cl bond-length disproportionation is observed in any of our results, implying no Jahn-Teller distortion in this system.

Due to the presence of inversion symmetry at the bond center and additional trigonal distortion in the $RuCl_6$ octahedra, the hopping integrals between the NN Ru t_{2g} Wannier orbitals have the following form [16,42]:

$$\hat{T} = \begin{pmatrix} t_1 & t_2 & t_4 \\ t_2 & t_1 & t_4' \\ t_4 & t_4' & t_3 \end{pmatrix},$$

where each hopping channel is displayed in Fig. 4 with the participating Ru t_{2g} Wannier orbitals therein. As shown in the

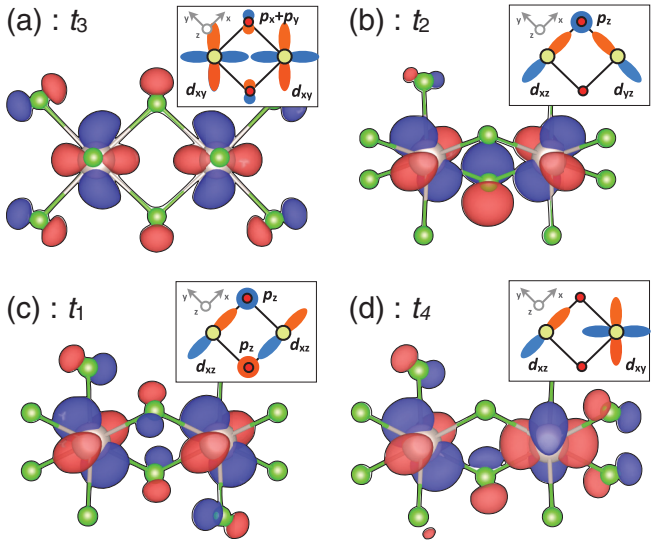

FIG. 4. Four major NN hopping channels—(a) t_3, (b) t_2, (c) t_1, and (d) t_4—within the t_{2g} subspace. For each hopping channel, the participating t_{2g} Wannier orbitals are plotted, where the schematics for each channel is represented in the inset. Note that the t_3 and t_2 terms depend more sensitively on the structural change than t_1 and t_2.

figure, while t_1 originates mainly from the δ- and σ-like d-d direct overlap integrals, t_2 is mostly from the π-type indirect overlap dominated by d-p-d hopping between the Ru and intervening Cl p orbitals. Note that the t_3 channel has both the d-d direct overlap and d-p-d indirect overlap, which have opposite signs to each other. Also, due to the small trigonal distortion, the small t_4 and t_4' terms are introduced, where the difference between them introduced by the monoclinic distortion is negligibly small.

Table I shows the hopping terms from the Wannier orbitals for four crystal structures optimized with different conditions. There is the old $P3_112$ structure [37] used in previous work, the structure with internal coordinates and lattice constants optimized with SOC, the structure with only internal coordinates optimized (fixed $a = a_0$ and $b = b_0$), and the one optimized with SOC, $U_{\rm eff}$, and the zigzag order. Hereafter, we denote the structures as cases 0 to III, respectively, as stated in Table I. With those optimized structures, calculations of the Wannier orbitals were performed without the inclusion of SOC, $U_{\rm eff}$, and magnetism. Surprisingly, the hopping integrals show a huge dependence on the structural change. In particular, the t_3 term varies from -0.229 to -0.062 eV depending on the structures, and t_2 also varies from 0.114 to 0.191 eV. Comparing the case 0 and II results, the effect of Cl relaxation is to enhance t_2 and suppress t_3. The effect of increasing Ru-Ru distance, which can be seen by comparing case I to III, is also similar to the role of Cl relaxation, with a less dramatic but still substantial trend. Such tendency can be understood from the character of participating Wannier orbitals shown in Fig. 4. The t_3 term, i.e., the most sensitive to the structural change, originates from the two distinct channels: one from the σ-like direct d-d overlap and another from the d-p-d indirect channel. The two channels has opposite sign to each other, with a minus sign for the d-d channel and plus sign for the d-p-d channel. As a result, enhancing the d-p-d channel by reducing the Ru-Cl distance or increasing the Ru-Cl-Ru angle will lead to better cancellation of the dominant d-d channel and reduction of the overall t_3 term, as shown in Table I. Enhancement of t_2 after Cl relaxation is also easy to understand since it mostly comes from the π-like d-p-d channel, while the t_3 dominated by the δ-like d-d channel is reduced as the Ru-Ru distance is increased. The trend for the small t_4 term is less clear, but it tends to enhance when there are more trigonal and monoclinic distortions.

TABLE I. Values of the averaged Ru-Cl distances, NN Ru-Ru distances, hopping integrals, and examples of exchange interactions for $U = 3$ eV and $J_{\rm H}/U = 0.15$ [16]. The structures of cases I to III were optimized with different stated conditions, while the case 0 structure is from Ref. [37]. In case II, lattice constants are fixed to be a_0 and b_0, while in cases I and III, they are allowed to relax. Hopping integrals and exchange interactions are shown in eV and meV units, respectively. For comparison, the values of hopping integrals and exchange interactions from the old structure (case 0) in Ref. [8] are listed.

	$d^{\rm avg}_{\rm Ru-Cl}$ (Å)	$d_{\rm Ru-Ru}$ (Å)	t_1 (eV)	t_2 (eV)	t_3 (eV)	t_4 (eV)	J (meV)	K (meV)	Γ (meV)	Γ' (meV)
Case 0 structure: old $P3_112$ structure (from Ref. [3], $a = a_0$, $b = b_0$)										
NN	2.45	3.44	+0.066	+0.114	−0.229	−0.010	−3.50	+4.60	+6.42	−0.04
Case I structure: $a = 0.981a_0$, $b = 0.986b_0$ (structure optimized with SOC)										
NN-Z	2.34	3.40	+0.058	+0.177	−0.154	−0.022	−2.67	−4.52	+7.27	−0.67
NN-X/Y		3.38	+0.060	+0.165	−0.160	−0.018	−2.81	−3.07	+6.99	−0.47
Case II structure: $a = a_0$, $b = b_0$ (structure optimized with SOC and lattice constants fixed)										
NN-Z	2.36	3.44	+0.044	+0.178	−0.109	−0.019	−1.49	−6.71	+5.28	−0.69
NN-X/Y		3.44	+0.042	+0.176	−0.107	−0.030	−1.55	−6.47	+5.24	−1.08
Case III structure: $a = 1.011a_0$, $b = 1.006b_0$ (structure optimized with SOC, $U_{\rm eff}$, and zigzag order)										
NN-Z	2.36	3.47	+0.036	+0.191	−0.062	−0.024	−0.74	−9.34	+3.71	−1.04
NN-X/Y		3.47	+0.037	+0.182	−0.075	−0.026	−1.09	−7.64	+4.38	−0.87

From the NN t_{2g} hopping terms, one can estimate the values of exchange interaction terms in the $j_{\rm eff} = 1/2$ spin Hamiltonian

$$\mathcal{H} = \sum_{\langle ij \rangle} \mathbf{S}_i \cdot \mathbf{M}_{ij} \cdot \mathbf{S}_j,$$

where the bond-dependent 3×3 matrix $\mathbf{M}_{ij}$ has the form

$$\mathbf{M} = \begin{pmatrix} J & \Gamma & \Gamma' \\ \Gamma & J & \Gamma' \\ \Gamma' & \Gamma' & J+K \end{pmatrix}.$$

Note that $\mathbf{M}_{ij}$ undergoes simultaneous cyclic permutations of rows and columns depending on the NN-bond directions. Explicit expressions for the Heisenberg J, the Kitaev K, and the symmetric anisotropy terms Γ and Γ' in terms of the hopping integrals U and the Hund's coupling $J_{\rm H}$ are reported in Refs. [16,42]. Using the values of t_i listed in Table I and setting $U = 3$ eV and $J_{\rm H}/U = 0.2$, we can calculate the values of exchange interactions which are listed in Table I. Note that changing the values of the U and $J_{\rm H}/U$ changes does not change the ratio between the exchange interactions when $J_{\rm H}/U > 0.05$. As shown in the table, among the exchange interactions, the Kitaev term shows dramatic change of changing sign after the Cl relaxation. This is due to the enhancement and suppression of the t_2 and t_3 terms. Increasing the Ru-Ru distance gradually enhances K and reduces J and Γ, which drives the system closer to the Kitaev spin-liquid limit with ferromagnetic K. Comparing cases II and III, note that increasing the lattice constant by 1% enhances the K term significantly. This implies the possibility of controlling the magnetism and realizing the Kitaev spin-liquid phase with a rather small amount of structural change such as epitaxial strain or uniaxial pressure. Another noticeable feature is the small but non-negligible Γ' term from the trigonal distortion, which can stabilize the experimentally observed zigzag order near the Kitaev spin-liquid phase with $K < 0$ [42].

Finally, we discuss the evolution of the magnetic moments' direction in the zigzag order with respect to structural changes. Figure 5(a) shows the schematic figure of the zigzag order with an angle of the moments θ with respect to the a axis. Note that in all of our calculations, the moments were residing on the ac plane. In the case 0 structure, both in the OpenMX and VASP results, the moments were parallel/antiparallel to the a axis (i.e., $\theta = 0$), consistent with our previous result [8]. After the structural optimization, the moments gain nonzero θ, which tends to increase when the lattice constant increases, as shown in Fig. 5(b). There is a difference in θ between the results from the two different codes, but the tendency of increasing the angle remains the same. We speculate that such behavior may originate from the Cl relaxation and the resulting change of exchange interactions, especially the change of the ratio between the K and Γ terms. Also, as the lattice constant is enlarged, the two zigzag chains with antiparallel moments in the unit cell begin to develop the difference in θ, resulting in the net ferromagnetic component in the ac plane. The origin of such behavior is unclear at this point.

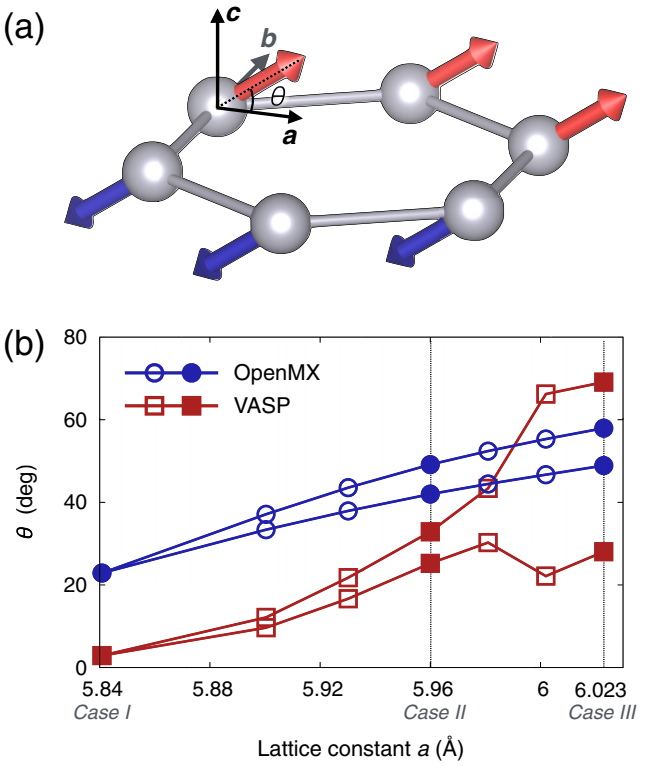

FIG. 5. (a) Schematic figure representing the zigzag magnetic order in the Ru honeycomb plane. Note that the moments are confined on the ac plane, where the angle of the moments with respect to the a axis is denoted as θ. (b) Evolution of θ for the two zigzag-ordered chains in the monoclinic unit cell as a function of a, obtained from OpenMX (blue) and VASP (red) codes. Structures with $a = 5.84$, 5.96, and 6.023 Å are cases I, II, and III, respectively, and angles from the structures are marked as filled symbols. The rest of the results are obtained from interpolation between the three structures, marked as empty symbols.

IV. STACKING WITHOUT $U_{\rm eff}$ AND MAGNETISM

Next let us study the stacking order of $RuCl_3$. First we discuss their relative total energies without including $U_{\rm eff}$ and magnetism. As mentioned in Sec. II, here we show the results using the PBEsol functional, and their comparison with vdW functional calculations is shown in the Appendix. Note that PBEsol results give the same lowest-energy configurations with other vdW results, and the closest c-axis constant to the experimentally observed one as well [3].

Figure 6 shows five unit cells we considered in this work, where the upper and lower panels show the side view of unit cells and the top view of Ru honeycomb layers, respectively. When we consider the Ru honeycomb as a triangular layer by ignoring Ru hollow sites, the α-$RuCl_3$ crystal structure can be understood as a stacking of Ru and Cl triangular layers with three triangular sublattices (a/A, b/B, and c/C, where capital and lowercase letters denote Ru and Cl layers, respectively) shown in Fig. 1(a) as a degree of freedom. In Fig. 6, each different structure can be understood as a sequence of sublattice indices. Note that within a $RuCl_3$ layer, any two Ru or Cl layers cannot be in the same sublattice. As we take into account Ru hollow sites, an additional degree of freedom

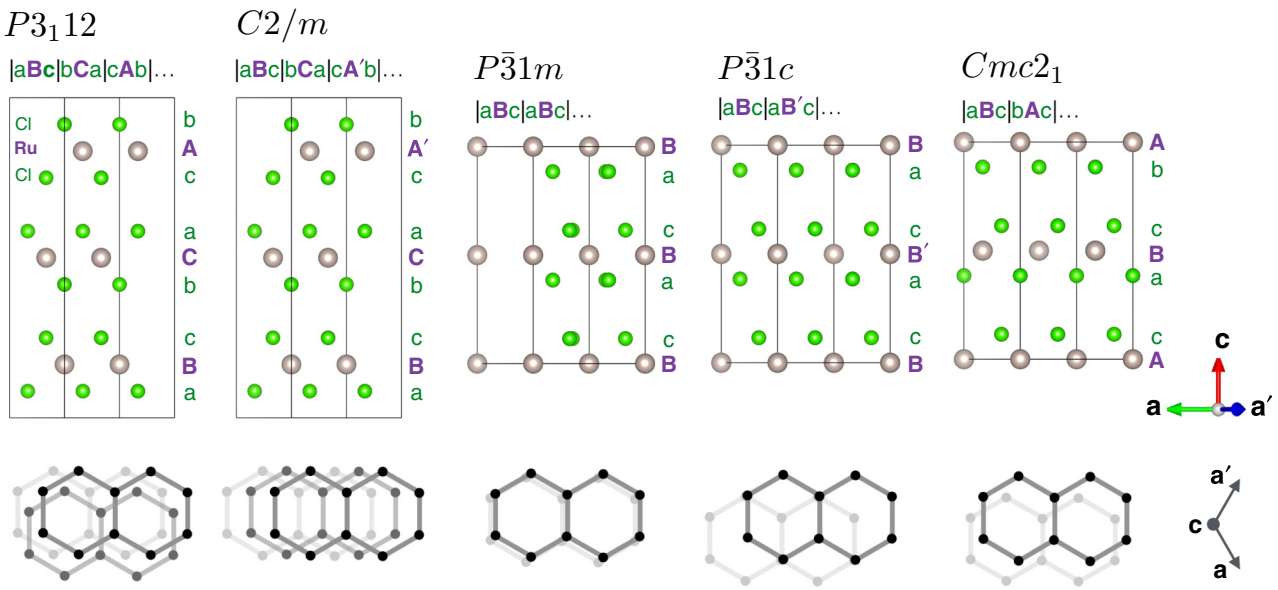

FIG. 6. Five different unit cells with two- and three-layer periodicity along the c direction. Upper and lower panels show the side view of the unit cell and schematic top view of Ru honeycomb stacking, respectively.

is introduced to each Ru layer, and we denote this with primes in the triangular sublattice index (for example, A, A′, and A″, as shown in the figure).

For structures with three-layer c-axis periodicity, we choose unit cells with $P3_112$ and $C2/m$ space groups. Note that the $C2/m$ structure was also reported as the space group of this compound [6,22], and is similar to the $P3_112$ structure. The major difference in the two structures is the c-axis ordering of the Ru honeycomb layers, where in the $C2/m$ unit cell, three Ru layers are related by translation by $(\mathbf{a}+\mathbf{a}^{'}+\mathbf{c})/3$, while in the $P3_112$ cell, they are related by a threefold screw axis. In addition, since the neutron-diffraction result identified a magnetic peak with two-layer c-axis periodicity at $T_{N1} = 14$ K in a polycrystalline sample [11], we consider two-layered unit cells as well. Avoiding two Cl^- triangular layers belonging to adjacent $RuCl_3$ layers locating on top of each other (i.e., sitting on the same triangular sublattice), we have only three unit cells with space groups $P\bar{3}1m$, $P\bar{3}1c$, and $Cmc2_1$, as shown in Fig. 6. Note that the $P\bar{3}1m$ cell is just a doubling of a single-layer unit cell, and the $P\bar{3}1c$ structure differs from the $P\bar{3}1m$ structure by the position of Ru hollow sites, so that half of the Ru sites avoid sitting on top of the Ru sites in the neighboring layer, as shown in the bottom panels of Fig. 6. Finally, the $Cmc2_1$ structure differs from other unit cells by anticyclic stacking of every other $RuCl_3$ layer, as shown in the stacking sequence in the figure, which can be obtained by applying a mirror operation to every other $RuCl_3$ layer.

TABLE II. Optimized lattice constants, relative total energies (ΔE) per formula unit (f.u.), and densities of states (DOS) at the Fermi level for five stacking unit cells. Values are obtained using PBEsol functional and including SOC, but without electron interactions.

	$P3_112$	$C2/m$	$P\bar{3}1m$	$P\bar{3}1c$	$Cmc2_1$
Lattice constants					
a/a_0	0.984	0.981	0.986	0.985	0.984
b/a_0	0.984	0.986	0.986	0.985	0.983
c/c_0	1.014	1.013	1.005	1.007	1.014
ΔE/f.u. (meV)	1.4	1.4	0.0	2.8	2.5
DOS at E_f (states/eV/f.u.)	9.2	7.9	6.0	10.8	8.5

Structure optimizations were performed including SOC, and Table II shows the optimized lattice constants with respect to experimentally reported lattice constants $a_0 = 5.96$ Å and $c_0 = 17.2$ Å and their relative total energies. Note that structures without threefold symmetry—monoclinic $C2/m$ and orthorhombic $Cmc2_1$—show slightly different a/a_0 and b/b_0. Among the five different structures, the $P\bar{3}1m$ structure yields the lowest energy. The $P3_112$ and $C2/m$ structures are closer in energy by 1.4 meV/f.u., and for the other phases, energy differences are less than 3 meV/f.u. compared to the the $P\bar{3}1m$ structure. The lowest energy of the $P\bar{3}1m$ structure can be attributed to the larger kinetic-energy gain originating from the larger band dispersion along the c direction compared to other structures. This is reflected in the lower DOS of the $P\bar{3}1m$ cell at the Fermi level compared to other structures, as shown in Table II and Fig. 7. Figure 7 presents total DOS for the five structures in the presence of SOC. Compared to the single-layer result depicted as the gray shaded areas in the figure, layer stacking yields pronounced peaks near the Fermi level except the $P\bar{3}1m$ structure in the results without SOC (not shown) due to the presence of flat bands along the c direction at the Fermi level. Inclusion of SOC smoothes the peaks, but the gross feature remains the same as shown in Fig. 7, which results in higher DOS at the Fermi level except the $P\bar{3}1m$ structure, as shown in Table II. Note that Stoner-type ferromagnetic (FM) instability is also observed, but in this study we concentrate on the experimentally observed zigzag magnetic order, as discussed in the next section.

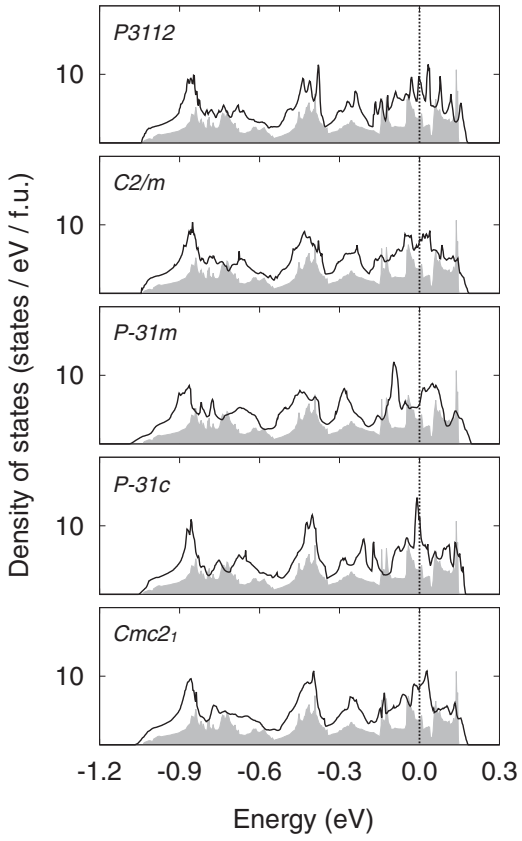

FIG. 7. Densities of states (DOS) for different α-$RuCl_3$ structures including SOC in the absence of U_{eff} and magnetism. The gray shaded areas show DOS of single-layer $RuCl_3$ multiplied by 0.5 as a reference.

V. STACKING WITH ZIGZAG MAGNETIC ORDER

Now we present the stacking results that include the on-site Coulomb interaction and magnetism. Figure 8 shows ten trial structural and magnetic configurations, where the direction of the magnetic moments in each layer is the same as the single-layer result in Sec. III. Fixing the in-plane zigzag order, we choose two interlayer magnetic configurations that we denote as cFM (ferromagnetic) and cAF (antiferromagnetic) hereafter. As shown in Fig. 8, in the cFM configuration, the zigzag-ordered layers are stacked along the c direction so that the FM zigzag chains in adjacent layers become closer in distance, while in the cAF configuration, the moments on one Ru layer are flipped. Note that there can be additional magnetic stacking orders due to the threefold rotational degree of freedom for each single-layer zigzag order— three different direction for FM zigzag chains—and in this work we chose the simplest configuration commensurate to the monoclinic unit cell [shown in Fig. 2(a)] for each structure. Structural optimizations were done first by varying the c axis with fixing a-lattice constants determined in the single-layer calculation, and later fully optimizing a- and c-axis constants and internal coordinates. Note that symmetry constraints are lost during the full optimizations including the Coulomb interaction and magnetism. As a result, the optimized structures slightly deviate from the original space-group symmetries, where the deviation develops in Cl positions with its size about 1% for each internal coordinate compared to the lattice constants. Note also that the structural optimization for each stacking with different magnetic configuration (either cFM or cAF configurations in Fig. 8) yielded negligible differences. All of the configurations become insulators with the gap of $\sim$1 eV between the lower and upper Hubbard bands at $U_{\text{eff}} = 2$ eV. The DOS for the resulting phases are almost identical to the one from the single-layer calculation [10] and show no significant difference compared to each other, so we do not present the DOS plots here.

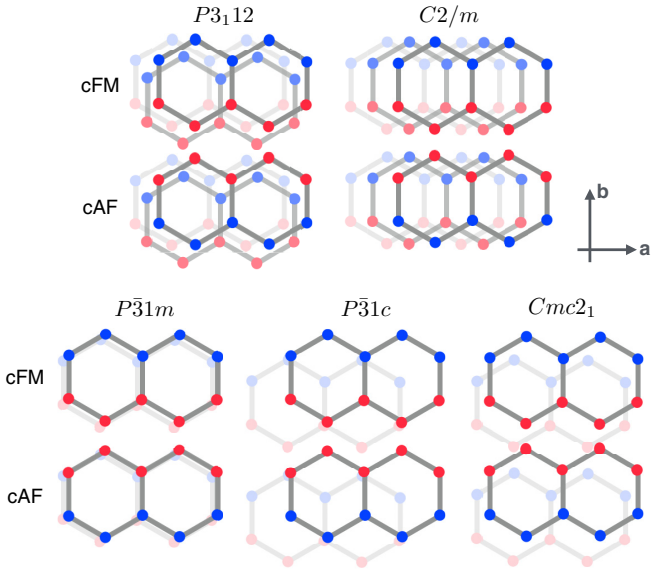

FIG. 8. Ten trial magnetic configurations with in-plane zigzag order, where the red and blue symbols depict Ru sites with antiparallel magnetic moments to each other.

Table III shows the optimization results. Compared to the results without stacking and magnetism, a few differences can be noticed: (i) Energy differences between structures are less than 1 meV per f.u., except the $P\bar{3}1m$ structure, which is higher in energy by $\sim$4.0 meV/f.u. compared to the other structures. Note that the $P\bar{3}1m$ structure showed the lowest energy in the calculation without U_{eff} and magnetism. With U_{eff} and magnetism introduced, the gap is fully opened for all of the structures and the relative energy gain in the $P\bar{3}1m$ structure due to the c-axis dispersion (discussed in Sec. IV)

TABLE III. Optimized lattice constants for five stacking unit cells, using the PBEsol functional and including SOC, U_{eff}, and magnetism. a, b, and c are the optimized monoclinic lattice constants (shown in Fig. 1) with a_0, b_0, and c_0 being their experimentally observed values, respectively [3].

	$P3_112$	$C2/m$	$P\bar{3}1m$	$P\bar{3}1c$	$Cmc2_1$
Lattice constants					
a/a_0	1.011	1.011	1.010	1.011	1.010
b/b_0	1.006	1.006	1.006	1.006	1.006
c/c_0	1.041	1.043	1.067	1.039	1.056
ΔE/f.u. (meV)					
cFM	0.4	0.1	3.7	0.8	0.0
cAF	0.4	0.2	4.1	0.9	0.4

becomes smaller. (ii) Energy differences between cFM and cAF configurations are smaller than 0.1 meV/f.u. for the $P3_112$, $C2/m$, and $P\bar{3}1c$ structures, and for the $P\bar{3}1c$ and $Cmc2_1$ stackings, the differences are about 0.4 meV/f.u. Such small energy differences can be attributed to weak interlayer exchange interactions, which will be discussed in the last paragraph of this section. (iii) Lattice constants are increased by 2 to 3% compared to the results without U_{eff}. (iv) Small monoclinic distortion, which manifests itself by the difference of a/a_0 and b/b_0 (and negative δ in Fig. 2), happens in every structure in the presence of the in-plane zigzag magnetic order.

Except for the $P\bar{3}1m$ structure which is higher in energy by ~4 meV/f.u. compared to other structures, the structural energy differences are smaller than 1 meV. This result implies the coexistence of different structures in experimentally synthesized samples. In particular, it is natural that the $P3_112$ and $C2/m$ structures have similar total energies; their only difference is the stacking of the Ru honeycomb order, which can be switched to each other by the ionic hopping of Ru atoms within the $RuCl_3$ layers. Indeed, both were reported as the crystal structure of α-$RuCl_3$ by different groups [3,11,22]. It is also interesting that the $Cmc2_1$ structure (with cFM order) shows the lowest energy, which can be transformed into other structures by applying mirror operations to every other $RuCl_3$ layer. One can speculate that the $Cmc2_1$ structure forms in the high-temperature regime and freezes below $T \sim 150$ K, where an anomalous behavior in magnetic susceptibility is observed [5,6], which contributes to the magnetic peak with two-layer periodicity in polycrystalline samples below $T_{N1} \simeq 14$ K [5,7,11].

Finally, we comment on the interlayer exchange interactions. Major interlayer hopping channels are shown in Fig. 9, where the largest channel is depicted as a green solid arrow, while others are represented as dashed/dotted arrows. Note that the value of the largest interlayer t_{2g} hopping term is about 35 meV, and magnitudes of other channels depicted in the figure are comparable to the largest one, i.e., about 20 to 30 meV. The interlayer exchange Heisenberg term is roughly estimated to be $J = t'^2/9U \sim 0.05$ meV for the $j_{\text{eff}} = 1/2$ pseudospins. This value is two-orders-of-magnitude smaller than the previously estimated in-plane exchange interactions in α-$RuCl_3$ [8,11], and is also consistent with the small energy differences between the cFM and cAF phases discussed above.

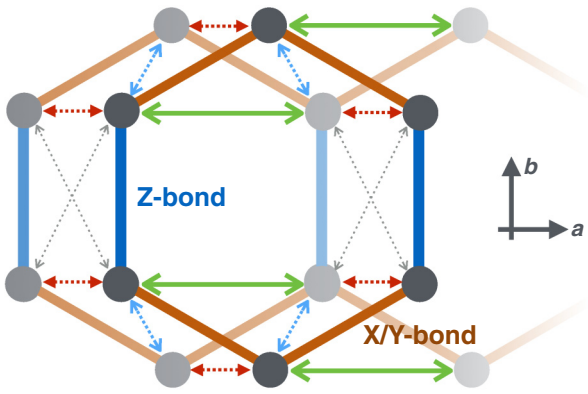

FIG. 9. Two distinct NN bonds— Z and X/Y bonds—in the presence of zigzag magnetic order, and the dominant interlayer hopping channels in $C2/m$ structure. Note that although the largest interlayer hopping channel is depicted as green thick and solid arrows, the magnitudes of all of the hopping channels in the figure are comparable to each other.

VI. DISCUSSION

The relative energies between different stacking order depends on the electronic structures of each system in our results, especially whether or not the system becomes fully insulating. Given that α-$RuCl_3$ remains insulating in the paramagnetic phase above T_{N1} with 1 eV of optical gap [4,10], we speculate that the four stacking orders—$P3_112$, $C2/m$, $P\bar{3}1c$, and $Cmc2_1$—are almost degenerate, as discussed in Sec. V.

The change of hopping integrals and exchange interaction terms after the structure optimization show that the physics of α-$RuCl_3$ is sensitive to the NN Ru-Ru distance and Cl position. For example, the strength of the Kitaev and Γ terms is significantly modified by the Ru-Ru and Ru-Cl distances. This implies that even a small amount of epitaxial tensile strain by 1% or uniaxial pressure perpendicular to the layer can significantly enhance the Kitaev term and push the system closer to the Kitaev limit. On the other hand, hydrostatic pressure or compressive strain can increase the t_3 term by decreasing the Ru-Ru distance. This reduces the FM Kitaev term and drives the effective model to the highly frustrated Γ-dominated regime. In addition, the presence of the negative Γ' term due to the trigonal distortion can stabilize the zigzag-ordered phase, as discussed in a previous study [42]. The effects of the monoclinic bond disproportionation [43] are another factor that can change the magnetism. In this regard, full experimental structure determination including precise atomic positions and stacking order would be important for future studies.

In summary, structural properties of α-$RuCl_3$ from *ab initio* calculations are presented in this study. SOC is found to prevent the Ru dimerization in the Ru honeycomb layers, and the presence of in-plane zigzag magnetic order further gives small monoclinic distortion. The relation between the hopping integrals and exchange interactions to the structure is also discussed. A total-energy comparison between different $RuCl_3$ stacking orders yields the $Cmc2_1$ and $C2/m$ structures to be the almost degenerate ground-state structures, and the $P3_112$ structure to be comparable in energy, with energy differences smaller than 0.4 meV per formula unit. In-plane exchange interactions are found to be sensitive to the structural distortions, and the $j_{\text{eff}} = 1/2$ pseudospin model is dominated by the FM Kitaev terms in the optimized structures with the presence of U_{eff}, similar to the two- and three-dimensional honeycomb iridates [44–46]. As expected, interlayer exchange interactions are estimated to be weak compared to the in-plane exchange interactions, so this system can be a good platform to study frustrated two-dimensional magnetism.

Note added. Recently, we became aware of the experimental work by Johnson and co-workers [47], which reports

monoclinic $C2/m$ crystal structure and the in-plane zigzag magnetic configuration with antiferromagnetic interplanar order below $T_N \sim 13$ K.

ACKNOWLEDGMENTS

We thank R. Coldea and S. Nagler for useful discussions. This work was supported by the NSERC of Canada and the Center for Quantum Materials at the University of Toronto. Computations were mainly performed on the GPC supercomputer at the SciNet HPC Consortium. SciNet is funded by the Canada Foundation for Innovation under the auspices of Compute Canada; the Government of Ontario; Ontario Research Fund - Research Excellence; and the University of Toronto.

APPENDIX: VAN DER WAALS CALCULATION

In this Appendix, we compare the results with using different exchange-correlation functionals including vdW interactions. Four functionals are considered: PBE, PBEsol, vdW-DF2 [48], and vdW-optB86b [49], where vdW-DF2 and vdW-optB86b functionals showed accuracies comparable to random-phase approximation (RPA) calculations in layered and bulk systems, respectively. Here, SOC, U_{eff}, and magnetism are not included.

Figure 10 shows the relative energies versus c-lattice constant with fixed $a = a_0$ for the results with four functionals, where $C2/m$ stacking order is not considered. Except PBE, which yields an unreasonably large value of c, the other three functionals yield $P\bar{3}1m$ and $P\bar{3}1c$ as configurations with the lowest and second-lowest energy. Compared to PBEsol, vdW functionals tend to yield a steeper energy curve away from the optimum c values and higher energy for the $P3_112$ phase.

Table IV shows the results from full lattice optimizations. Except for the change of a-lattice constants, where vdW-DF2 results yield 3% enhancement of the a value, the features are qualitatively similar to the results in Fig. 10. $P\bar{3}1m$ is still the most favored configuration, and optimized c-lattice constants do not change significantly from the values in Fig. 10. It is notable that the vdW results give high energies for the $P3_112$ and $Cmc2_1$ phases, which were the favored phases in PBEsol+SOC+U_{eff} calculations.

Compared to the vdW functionals, PBEsol yields reasonable estimates of total energy and lattice constants, although quantitative differences can be noticed. Since test calculations on combining vdW functionals and DFT+SOC+U, which is crucial in understanding the physics of $RuCl_3$, have not been done yet, in this study the PBEsol functional is employed for the rest of the calculations.

TABLE IV. Optimized lattice constants and total-energy differences for four stacking orders, using the PBE, PBEsol, vdW-DF2, and vdW-optB86b functionals. SOC is not included in these calculations.

	$P3_112$	$P\bar{3}1m$	$P\bar{3}1c$	$Cmc2_1$
a/a_0				
PBE	1.011	1.012	1.006	1.000
PBEsol	0.984	0.986	0.985	0.984
vdW-DF2	1.027	1.029	1.030	1.027
vdW-optB86b	1.000	1.000	1.000	1.000
c/c_0				
PBE	1.098	1.091	1.132	1.140
PBEsol	1.014	1.005	1.007	1.014
vdW-DF2	1.015	1.004	1.001	1.010
vdW-optB86b	0.980	0.980	0.980	0.980
ΔE/f.u. (meV)				
PBE	1.4	0.0	2.6	4.5
PBEsol	2.1	0.0	3.0	2.3
vdW-DF2	10.5	0.0	1.0	7.0
vdW-optB86b	9.9	0.0	2.3	7.1

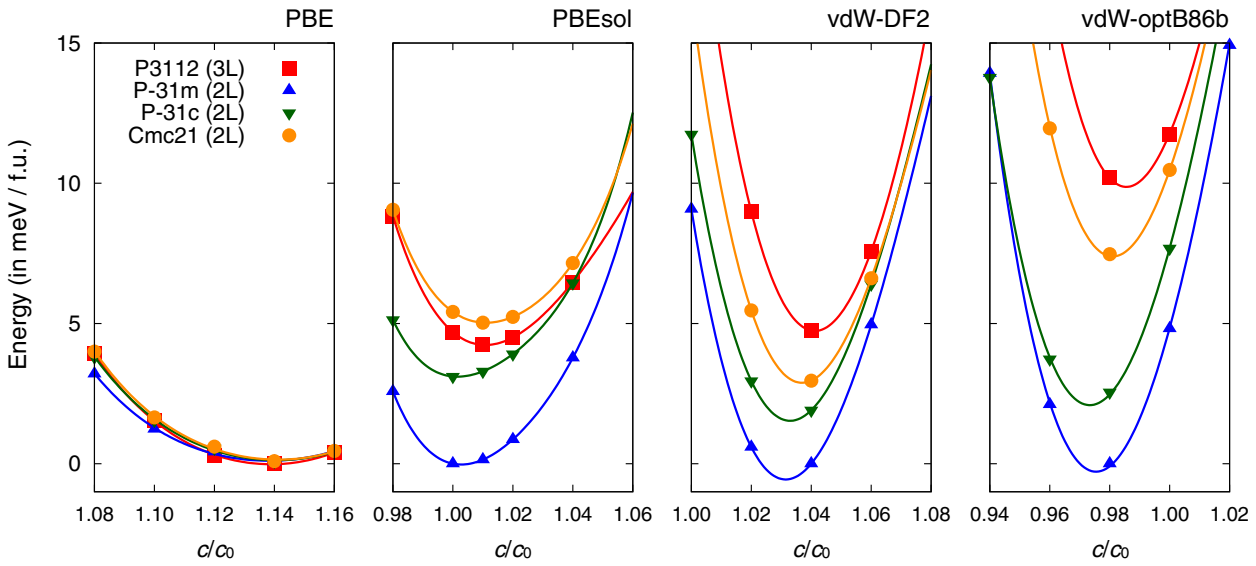

FIG. 10. Total energy vs c-lattice constant plots with fixed $a = a_0 = 5.96$ Å for different crystal structure and exchange-correlation functionals. From left to right, results with PBE, PBEsol, vdW-DF2, and vdW-optB86b functionals are shown.

[1] W. Witczak-Krempa, G. Chen, Y. B. Kim, and L. Balents, Annu. Rev. Condens. Matter Phys. **5**, 57 (2014).

[2] J. G. Rau, E. K.-H. Lee, and H.-Y. Kee, Annu. Rev. Condens. Matter Phys. **7**, 1 (2016).

[3] E. V. Stroganov and K. V. Ovchinnikov, Ser. Fiz. Khim. **12**, 152 (1957).

[4] K. W. Plumb, J. P. Clancy, L. J. Sandilands, V. V. Shankar, Y. F. Hu, K. S. Burch, H.-Y. Kee, and Y.-J. Kim, Phys. Rev. B **90**, 041112(R) (2014).

[5] J. A. Sears, M. Songvilay, K. W. Plumb, J. P. Clancy, Y. Qiu, Y. Zhao, D. Parshall, and Y.-J. Kim, Phys. Rev. B **91**, 144420 (2015).

[6] Y. Kubota, H. Tanaka, T. Ono, Y. Narumi, and K. Kindo, Phys. Rev. B **91**, 094422 (2015).

[7] M. Majumder, M. Schmidt, H. Rosner, A. A. Tsirlin, H. Yasuoka, and M. Baenitz, Phys. Rev. B **91**, 180401 (2015).

[8] H.-S. Kim, Vijay Shankar V., A. Catuneanu, and H.-Y. Kee, Phys. Rev. B **91**, 241110(R) (2015).

[9] L. J. Sandilands, Y. Tian, K. W. Plumb, Y.-J. Kim, and K. S. Burch, Phys. Rev. Lett. **114**, 147201 (2015).

[10] L. J. Sandilands, Y. Tian, A. A. Reijnders, H.-S. Kim, K. W. Plumb, Y.-J. Kim, H.-Y. Kee, and K. S. Burch, Phys. Rev. B **93**, 075144 (2016).

[11] A. Banerjee, C. A. Bridges, J.-Q. Yan, A. A. Aczel, L. Li, M. B. Stone, G. E. Granroth, M. D. Lumsden, Y. Yiu, J. Knolle, S. Bhattacharjee, D. L. Kovrizhin, R. Moessner, D. A. Tennant, D. G. Mandrus, and S. E. Nagler, Nature Materials (2016), doi:10.1038/nmat4604.

[12] F. Ye, S. Chi, H. Cao, B. C. Chakoumakos, J. A. Fernandez-Baca, R. Custelcean, T. F. Qi, O. B. Korneta, and G. Cao, Phys. Rev. B **85**, 180403 (2012).

[13] H. Gretarsson, J. P. Clancy, X. Liu, J. P. Hill, E. Bozin, Y. Singh, S. Manni, P. Gegenwart, J. Kim, A. H. Said, D. Casa, T. Gog, M. H. Upton, H.-S. Kim, J. Yu, V. M. Katukuri, L. Hozoi, J. van den Brink, and Y.-J. Kim, Phys. Rev. Lett. **110**, 076402 (2013).

[14] M. J. O'Malley, H. Verweij, and P. M. Woodward, J. Solid State Chem. **181**, 1803 (2008).

[15] Y. Singh, S. Manni, J. Reuther, T. Berlijn, R. Thomale, W. Ku, S. Trebst, and P. Gegenwart, Phys. Rev. Lett. **108**, 127203 (2012).

[16] J. G. Rau, Eric K.-H. Lee, and H.-Y. Kee, Phys. Rev. Lett. **112**, 077204 (2014).

[17] A. Kitaev, Ann. Phys. **321**, 2 (2006).

[18] G. Jackeli and G. Khaliullin, Phys. Rev. Lett. **102**, 017205 (2009).

[19] Y. Miura, Y. Yasui, M. Sato, N. Igawa, and K. Kakurai, J. Phys. Soc. Jpn. **76**, 033705 (2007).

[20] S. A. J. Kimber, I. I. Mazin, J. Shen, H. O. Jeschke, S. V. Streltsov, D. N. Argyriou, R. Valentí, and D. I. Khomskii, Phys. Rev. B **89**, 081408(R) (2014).

[21] J. M. Fletcher, W. E. Gardner, A. C. Fox, and G. Topping, J. Chem. Soc. A, 1038 (1967).

[22] K. Brodersen, G. Thiele, H. Ohnsorge, I. Recke, and F. Moers, J. Less-Common Met. **15**, 347 (1968).

[23] S. K. Choi, R. Coldea, A. N. Kolmogorov, T. Lancaster, I. I. Mazin, S. J. Blundell, P. G. Radaelli, Y. Singh, P. Gegenwart, K. R. Choi, S.-W. Cheong, P. J. Baker, C. Stock, and J. Taylor, Phys. Rev. Lett. **108**, 127204 (2012).

[24] G. Kresse and J. Hafner, Phys. Rev. B **47**, 558 (1993).

[25] G. Kresse and J. Furthmüller, Phys. Rev. B **54**, 11169 (1996).

[26] P. E. Blöchl, O. Jepsen, and O. K. Andersen, Phys. Rev. B **49**, 16223 (1994).

[27] S. L. Dudarev, G. A. Botton, S. Y. Savrasov, C. J. Humphreys, and A. P. Sutton, Phys. Rev. B **57**, 1505 (1998).

[28] J. P. Perdew, A. Ruzsinszky, G. I. Csonka, O. A. Vydrov, G. E. Scuseria, L. A. Constantin, X. Zhou, and K. Burke, Phys. Rev. Lett. **100**, 136406 (2008).

[29] J. He, K. Hummer, and C. Franchini, Phys. Rev. B **89**, 075409 (2014).

[30] N. Marzari and D. Vanderbilt, Phys. Rev. B **56**, 12847 (1997).

[31] I. Souza, N. Marzari, and D. Vanderbilt, Phys. Rev. B **65**, 035109 (2001).

[32] A. A. Mostofi, J. R. Yates, Y.-S. Lee, I. Souza, D. Vanderbilt, and N. Marzari, Comput. Phys. Commun. **178**, 685 (2003).

[33] T. Ozaki, Phys. Rev. B **67**, 155108 (2003).

[34] M. J. Han, T. Ozaki, and J. Yu, Phys. Rev. B **73**, 045110 (2006).

[35] D. M. Ceperley and B. J. Alder, Phys. Rev. Lett. **45**, 566 (1980).

[36] J. P. Perdew and A. Zunger, Phys. Rev. B **23**, 5048 (1981).

[37] E. Stroganov and K. Ovchinnikov, Vestnik. Leningrad. Univ., Ser. Fiz. Khim. **12**, 152 (1957).

[38] J. P. Perdew, K. Burke, and M. Ernzerhof, Phys. Rev. Lett. **77**, 3865 (1996).

[39] B. J. Kim, H. Jin, S. J. Moon, J.-Y. Kim, B.-G. Park, C. S. Leem, J. Yu, T. W. Noh, C. Kim, S.-J. Oh, J.-H. Park, V. Durairaj, G. Cao, and E. Rotenberg, Phys. Rev. Lett. **101**, 076402 (2008).

[40] B. Kim, H. Ohsumi, T. Komesu, S. Sakai, T. Morita, H. Takagi, and T. Arima, Science **323**, 1329 (2009).

[41] G.-Q. Liu, V. N. Antonov, O. Jepsen, and O. K. Andersen, Phys. Rev. Lett. **101**, 026408 (2008).

[42] J. G. Rau and H.-Y. Kee, arXiv:1408.4811.

[43] I. Kimchi, R. Coldea, and A. Vishwanath, Phys. Rev. B **91**, 245134 (2015).

[44] Y. Yamaji, Y. Nomura, M. Kurita, R. Arita, and M. Imada, Phys. Rev. Lett. **113**, 107201 (2014).

[45] V. M. Katukuri, S. Nishimoto, V. Yushankhai, A. Stoyanova, H. Kandpal, S. Choi, R. Coldea, I. Rousochatzakis, L. Hozoi, and J. van den Brink, New J. Phys. **16**, 013056 (2014).

[46] H.-S. Kim, E. K.-H. Lee, and Y. B. Kim, Europhys. Lett. **112**, 67004 (2015).

[47] R. D. Johnson, S. C. Williams, A. A. Haghighirad, J. Singleton, V. Zapf, P. Manuel, I. I. Mazin, Y. Li, H. O. Jeschke, R. Valentí, and R. Coldea, Phys. Rev. B **92**, 235119 (2015).

[48] K. Lee, E. D. Murray, L. Kong, B. I. Lundqvist, and D. C. Langreth, Phys. Rev. B **82**, 081101 (2010).

[49] J. Klimeš, D. R. Bowler, and A. Michaelides, Phys. Rev. B **83**, 195131 (2011).